Experimental Eye Research 186 (2019) 107713

Contents lists available at ScienceDirect

Experimental Eye Research

journal homepage: www.elsevier.com/locate/yexer

A longitudinal study of retinopathy in the PEX1-Gly844Asp mouse model for mild Zellweger Spectrum Disorder

Catherine Argyriou[a,*,2], Anna Polosa[b,2], Bruno Cecyre[c], Monica Hsieh[d], Erminia Di Pietro[d], Wei Cui[d], Jean-François Bouchard[c], Pierre Lachapelle[b,d,1], Nancy Braverman[a,d,e,1]

[a] Department of Human Genetics, McGill University, Research Institute of the McGill University Health Centre, 1001 Decarie Boulevard, Montreal, Quebec, H4A 3J1, Canada
[b] Department of Ophthalmology, McGill University, 1001 Decarie Boulevard, Montreal, Quebec, H4A 3J1, Canada
[c] School of Optometry, Université de Montréal, Pavillon 3744 Jean-Brillant, Bureau 260-39, Montréal, Québec, H3T 1P1, Canada
[d] Child Health and Human Development Program, Research Institute of the McGill University Health Centre, 1001 Decarie Boulevard, Montreal, Quebec, H4A 3J1, Canada
[e] Department of Pediatrics, 1001 Decarie Boulevard, Montreal, Quebec, H4A 3J1, Canada

ARTICLE INFO

Keywords:
Peroxisome disorders
Zellweger spectrum disorder
PEX1
Pex1 mouse model
Retinal degeneration

ABSTRACT

Zellweger Spectrum Disorder (ZSD) is an autosomal recessive disease caused by mutations in any one of 13 *PEX* genes whose protein products are required for peroxisome assembly. Retinopathy leading to blindness is one of the major untreatable handicaps faced by patients with ZSD but is not well characterized, and the requirement for peroxisomes in retinal health is unknown. To address this, we examined the progression of retinopathy from 2 to 32 weeks of age in our murine model for the common human PEX1-p.Gly843Asp allele (PEX1-p.Gly844Asp) using electrophysiology, histology, immunohistochemistry, electron microscopy, biochemistry, and visual function tests. We found that retinopathy in male and female PEX1-G844D mice was marked by an attenuated cone function and abnormal cone morphology early in life, with gradually decreasing rod function. Structural defects at the inner retina occurred later in the form of bipolar cell degradation (between 13 and 32 weeks). Inner segment disorganization and enlarged mitochondria were seen at 32 weeks, while other inner retinal cells appeared preserved. Visual acuity was diminished by 11 weeks of age, while signal transmission from the retina to the brain was relatively intact from 7 to 32 weeks of age. Molecular analyses showed that PEX1-G844D is a subfunctional but stable protein, contrary to human PEX1-G843D. Finally, C26:0 lysophosphatidylcholine was elevated in the PEX1-G844D retina, while phopshoethanolamine plasmalogen lipids were present at normal levels. These characterization studies identify therapeutic endpoints for future preclinical trials, including improving or preserving the electroretinogram response, improving visual acuity, and/or preventing loss of bipolar cells.

1. Introduction

Peroxisomes are ubiquitous organelles numbering up to several hundred per mammalian cell, each containing over 50 matrix enzymes required for multiple vital metabolic pathways (Wanders and Waterham, 2006). In mammals, 16 PEX proteins, encoded by *PEX* genes, regulate peroxisome biogenesis, which includes synthesis, assembly, matrix protein import, and division. Primarily biallelic mutations in any of 13 *PEX* genes result in Zellweger Spectrum Disorder (ZSD), a heterogeneous group of disorders with a range of multi-system manifestations (Argyriou et al., 2016; Falkenberg et al., 2017). Phenotypic severity in ZSD is associated with the level of residual PEX protein activity and consequent peroxisome function. Mutations in *PEX1* are the most common cause, accounting for roughly 70% of known North American patients, with one mutation, *PEX1*-c.[2528G > A] representing roughly 30% of all ZSD alleles (Reuber et al., 1997; Steinberg et al., 2004; Ebberink et al., 2011). *PEX1*-c.[2528G > A] encodes the missense protein PEX1-p.[Gly843Asp] (or

* Corresponding author. Research Institute of the McGill University Health Centre, 1001 Decarie Boulevard, EM0.3211, Montreal, QC, H4A 3J1, Canada.
E-mail addresses: Catherine.argyriou@mail.mcgill.ca (C. Argyriou), anna.polosa@mail.mcgill.ca (A. Polosa), bruno.cecyre@umontreal.ca (B. Cecyre), monica.hsieh@mail.mcgill.ca (M. Hsieh), erminia.di_pietro@mail.mcgill.ca (E. Di Pietro), wei.cui@mail.mcgill.ca (W. Cui), jean-francois.bouchard@umontreal.ca (J.-F. Bouchard), pierre.lachapelle@mcgill.ca (P. Lachapelle), Nancy.braverman@mcgill.ca (N. Braverman).
[1] Co-last authors.
[2] These authors contributed equally.

https://doi.org/10.1016/j.exer.2019.107713
Received 22 March 2019; Received in revised form 17 May 2019; Accepted 25 June 2019
Available online 27 June 2019

G843D), and results in a milder ZSD phenotype without developmental defects, rather a progressive disorder due to ongoing peroxisome dysfunction (Collins and Gould, 1999; Gärtner et al., 1999; Preuss et al., 2002).

PEX1 and its partner protein PEX6 are AAA ATPases that form part of the peroxisome 'exportomer' complex. The PEX1-PEX6 complex is anchored to the peroxisome membrane by PEX26 and uses the energy from ATP hydrolysis to remove the PEX5 enzyme receptor from the peroxisome membrane so that it can be recycled for additional rounds of import (Schwerter et al., 2017). If not recycled, PEX5 is targeted for proteasomal degradation (Kiel et al., 2005), and enzyme import into the peroxisome is impaired.

Although the clinical presentation of ZSD is highly variable and can include brain, liver, adrenal, and bone involvements (Argyriou et al., 2016), nearly all patients develop a progressive retinopathy leading to blindness. In severely affected patients, ophthalmic manifestations can include, in addition to retinopathy, glaucoma and corneal clouding (Folz and Trobe, 1991). Cataracts can develop with age in some patients (Ebberink et al., 2010). Across the disease spectrum, however, posterior segment abnormalities, particularly photoreceptor loss, are the most severe of all ophthalmic manifestations (Folz and Trobe, 1991). On the milder end of the spectrum, patients have been diagnosed with Usher Syndrome (Zaki et al., 2016; Neuhaus et al., 2017), and presentations are usually characterized by retinitis pigmentosa, macular atrophy, reduced visual acuity, and reduced or extinguished electroretinograms (Majewski et al., 2011; Berendse et al., 2016; Ratbi et al., 2016). Additional descriptions include retinal arteriolar attenuation, optic nerve atrophy, nystagmus, and foveal thinning. More detailed descriptions over time of two individuals homozygous for PEX1-G843D report progressive peripheral visual field loss, nyctalopia, dyschromatopsia (Pakzad-Vaezi and Maberley, 2014), diminished photoreceptor function, cystoid macular edema and macular degeneration (Ventura et al., 2016).

To understand the course and mechanism of peroxisome-mediated visual deterioration in ZSD, and to guide future therapeutic studies, we engineered a knock-in mouse model which has the PEX1-G843D equivalent murine mutation (PEX1-G844D). Initial phenotyping of this model showed diminished full-field flash electroretinograms (ffERG) at 2–4 months. Reduced staining of cone photoreceptors was observed at 3 wks of age and became more prominent at 22 wks of age (Hiebler et al., 2014). Gene expression studies showed decreased cone-specific genes *Arr3*, *Pde6h*, *Gnat2*, and *Opn1mw*, and increased *Cyp4a14*, involved in omega oxidation of fatty acids and *Ufd1l*, involved in endoplasmic reticulum-associated degradation and cholesterol metabolism. In this manuscript, we greatly expand the characterization of the structural and functional consequences of the PEX1-G844D mutation on the mouse retina using electrophysiology (ffERG and visual evoked potential: VEP), visual acuity measurements (optokinetic reflex, OKR), peroxisome protein levels and localization, and biochemical metabolite measurements. We examine retinal structure and cell types using histology, immunohistochemistry, and electron microscopy. Furthermore, we provide a time course of disease progression to identify endpoints for preclinical interventions. The results obtained allowed us to identify the onset of this severe retinal degeneration as well as better document its final stage, and provide the first in-depth ophthalmological characterization in any peroxisome-deficient model over time.

2. Materials and methods

2.1. Animal husbandry

All animal experiments comply with the National Institutes of Health guide for the care and use of Laboratory animals (NIH Publications No. 8023, revised 1978). PEX1-G844D mice were maintained on a mixed 129/SvEv and C57BL/6N Taconic background. Strain background was evaluated by SNP genotyping (MaxBax, Charles River, Wilmington, MA) and showed a stable 70% 129/SvEv and 30% C57BL/6N Taconic. Mice were housed at the RI-MUHC Glen site animal care facility with *ad libitum* access to food and water. All experiments were performed at the RI-MUHC Glen site, except visual acuity measures which were performed at the Pavillon Liliane-de-Stewart de l'Université de Montréal animal care facility. All experiments were approved by the RI-MUHC Animal Care Committee or the Université de Montréal Ethics Committee. Euthanasia was performed by CO_2 under isoflurane anaesthesia (5% isoflurane in oxygen until loss of consciousness, immediately followed by CO_2 at maximum flow rate, 4 LPM). Both males and females were used for all experiments, and wild-type and PEX1-G844D heterozygous mice used as littermate controls. There were no phenotypic differences based on sex or control genotype.

2.2. Genotyping

For routine genotyping, genomic DNA was isolated from ear punches of 21-day-old mice by incubating in 75 µl alkaline lysis buffer (25 mM NaOH, 0.2 mM Na_2EDTA) at 95 °C for 20 min, then neutralized with 250 µl 40 mM Tris-HCl. Genotypes were determined by PCR amplification (forward primer 5′-TCAATGTGTCCAGCACCTTC-3'; reverse primer 5′-TATGGAACGGAATGAGGC-3′). The *Pex1* c.2531G > A (PEX1 p.Gly844Asp) allele yields a 852 base pair product and the wild-type allele yields a 672 base pair product (size difference reflects the residual *Neo* cassette fragment in intron 13 (Hiebler et al., 2014)).

2.3. Visual electrophysiology

2.3.1. Full-field flash electroretinogram (ffERG)

Retinal function was assessed using ffERG as previously described (Polosa et al., 2017). Briefly, after 12 h dark adaptation, mice were anesthetized [intraperitoneal injection of 130 mg ketamine, 13 mg xylazine in sterile PBS per kg body weight] and their pupils dilated [1% Mydriacyl Tropicamide (Alcon, Mississauga, Canada)]. Procedures were performed in a dark room under a dim red light illumination. Body temperature was maintained at 37 °C (homeothermic heating blanket, Harvard Apparatus, Holliston, MA). Full field ERG recordings (bandwidth: 1–1000 Hz; 10 000 X; 6 db attenuation; Grass P-511 amplifiers; Grass Instruments, Quincy, MA) and oscillatory potentials (OPs) (bandwidth: 100–1000 Hz; 50 000X; 6 db attenuation; Grass P511 amplifiers; Grass Instruments, Quincy, MA) were performed simultaneously with the Biopac data acquisition system (Biopac MP 100 WS, Biopac System Inc., Goleta, CA) using a DTL fibre electrode (27/7 X-Static® silver coated conductive nylon yarn, Sauquoit Industries, Scranton, PA) placed on the cornea and held in place with Tear-Gel (Novartis Ophthalmic, Novartis Pharmaceuticals Inc, Canada). The reference electrode (Grass E5 disc electrode; Grass Instruments, Quincy, MA) was positioned in the mouth and the ground electrode (Grass E2 subdermal electrode; Grass Instruments, Quincy, MA) inserted in the tail. Scotopic ERGs and OPs were obtained from fully dark-adapted retinas in response to progressively brighter flashes of white light ranging in luminous intensity from -6.3 log cd.s.m^{-2} to -1.5 log cd.s.m^{-2} in 0.9 log-unit increments, and from -1.5 log cd.s.m^{-2} to 0.9 log cd.s.m^{-2} in 0.3 log-unit increments [Grass PS-22 photostimulator (Grass Instruments; Quincy, MA), inter-stimulus interval: 10 s, flash duration 20 µs, average of 3–5 flashes depending on luminance]. Photopic ERGs and OPs were evoked to flashes of 0.9 log cd.s.m^{-2} (photopic background, 30 cd m^{-2}, interstimulus interval: 1 s, flash duration 20 µs, average of 20 flashes). In order to avoid any light adaptation effect, the photopic recordings were obtained 20 min following the opening of the background light (Molotchnikoff et al., 1987; Peachey et al., 1993). Mice were always tested within 3 h of their daylight onset.

The amplitudes of the a-wave, b-wave and oscillatory potentials (OPs) were measured as previously described (Joly et al., 2006). Briefly, the amplitude of the a-wave was measured from the baseline to the most negative trough, while the amplitude of the b-wave was

measured from the trough of the a-wave to the most positive peak of the ERG (scotopic ERG) and from the baseline to the highest peak of the b-wave (photopic ERG). OP amplitude was measured individually from the trough to the peak and the resulting values were summed to yield the sum of OPs (SOPs) variable. For each parameter, the amplitude value had to be twice the amplitude of the noise level (calculated prior to flash stimulation) to be considered a response. Peak times were measured from flash onset to respective waveform.

2.3.2. Visual evoked potential (VEP)

Retinocortical function was assessed by measuring the VEP as previously described (Jung et al., 2015). An active electrode (Grass E2 subdermal electrode) was inserted subcutaneously over the occipital cortex (lambda stereotaxic coordinate as per (Swanson, 2004)), while the ground and the reference electrodes remained at the same location as the ffERG recordings. VEPs (bandwidth: 1–100 Hz, 10 000X; 6 db attenuation; Grass P-511 amplifiers) were evoked to flashes of 0.9 log cd.s.m^{-2} (interstimulus interval: 1 s, flash duration 20 μs, average of 100 flashes; background light at 30 cd m^{-2}). Only the left eye was stimulated. Two components could be identified on VEP tracings: a negative (N1) and a positive (P1). The N1 value was measured from baseline to the most negative trough, and the P1 value from N1 to the most positive peak. Latency was measured from flash onset to trough (N1) or peak (P1). Concurrent photopic ffERG was recorded on all animals that underwent VEP recording.

2.4. Assessing visual acuity with the virtual optomotor system

The visual acuity of mice was determined using a virtual-reality optomotor system (CerebralMechanics, Lethbridge, Canada) as previously described (Prusky et al., 2004). Briefly, freely moving mice were placed on an elevated platform and exposed to vertical sine wave gratings (spatial frequencies varying from 0.01 to 0.5 cycles/degree; 100% contrast) rotating at 12°/sec. When detecting the stimulus, the mouse would normally stop its exploratory activities and track the grating with reflexive head movements in concert with the rotation. The spatial frequency of the grating was gradually increased until the mice no longer exhibited a tracking behavior. The highest spatial frequency that could be followed determined the visual acuity (in cycles per degree) for each eye. This technique yields independent measures of right- and left-eye acuity, as only motion in the temporal-to-nasal direction evokes a tracking response. Mice were always tested within 3 h of their daylight onset. Each mouse was tested twice and the average visual acuity from both eyes per test was calculated.

2.5. Lipid analysis

For liquid chromatography-tandem mass spectrometry (LC-MS/MS) analysis, retinas were homogenized in PBS using a mini pestle. 2:1 chloroform/methanol containing 0.05% butylhydroxytoluene (BHT) was added to 50 μg protein extract in a glass tube and incubated on an orbital shaker at room temperature for 2 h. Samples were centrifuged at 2500 rpm for 10 min and the supernatant was transferred to a clean glass tube. The supernatant was washed with 0.2 vol of purified water, mixed and centrifuged at 2000 rpm room temperature for 5 min to separate the two phases. The upper phase was removed and the lower phase was washed with Folch theoretical upper phase (3:48:47 chloroform:methanol:water). Samples were mixed and centrifuged at 2000 rpm for 5 min and the upper phase was removed. The lower phase was dried under nitrogen and then in a vacuum desiccator for 30 min. The dried lipid was dissolved in 3:2 hexane:isopropanol containing 10 ng each of internal standard, 16:0-D4 lyso-PAF (20.6 pmol) and D4-26:0-lyso-PC (15.6 pmol). Samples were filtered by centrifugation (Corning (Tewksbury, MA) Costar spin-X centrifuge tube filters) for 5 min. Filtrates were analyzed in Verex auto-sampler vials (Phenomenex, Torrance, CA). A 2.1 × 50 mm, 1.7 μm chromatography column and a Waters (Milford, MA) TQD (Triple Quadrupole Mass Spectrometer) interfaced with an Acquity UPLC (ultra-performance liquid chromatography) was used in positive ion electrospray (ESI)-MS/MS ionization. The solvent systems were: mobile phase A = 54.5% water/45% acetonitrile/0.5% formic acid, mobile phase B = 99.5% acetonitrile/0.5% formic acid with both solutions containing 2 mM ammonium formate. Injections of extracts dissolved in 3:2 isopropanol/hexane were made with initial solvent conditions of 85% mobile phase A/15% mobile phase B. The gradient employed was from 15% to 100% mobile phase B over a period of 2.5 min, held at 100% mobile phase B for 1.5 min before reconditioning the column back to 85% mobile phase A/15% mobile phase B for 1 min at a solvent rate of 0.7 ml/min. A column temperature of 35 °C and an injection volume of 5 μl for plasmalogen and 10 μl for lysoPC were used for analysis. Ethanolamine plasmalogens were detected by multiple reaction monitoring (MRM) transitions representing fragmentation of [M + H]+ species to m/z 311, 339, 361, 385, 389, 390 for compounds with 16:1, 18:1, 20:4. 22:6, 22:4, and 18:0, at the sn-2 position, respectively. Lysophosphatidylcholine (LysoPC) species were detected by multiple reaction monitoring (MRM) transitions representing fragmentation of [M + H]+ species to m/z 104. Reagents used were authentic plasmalogen standards, tetradeuterated internal standards 26:0-D4 lysoPC (Avanti Polar Lipids, Alabaster, AL), 16:0-D4 lyso PAF (Cayman Chemical Company, Ann Arbor, MI) and HPLC grade solvents (methanol, acetonitrile, chloroform, water) (Fisher Scientific, Waltham, MA), formic acid (Honeywell Fluka), ammonium formate (Sigma-Aldrich, St. Louis, MO), and PBS (Thermo Fisher Scientific, Waltham, MA).

2.6. Immunoblotting and immunofluorescent microscopy

2.6.1. Mouse retinas were homogenized in IGEPAL lysis buffer

Lysates (20 μg) were separated on 7.5% polyacrylamide gel, transferred to nitrocellulose membranes, and hybridized in 5% milk with primary antibodies: 1:1000 rabbit anti-human PEX1 (Proteintech 13669-1-AP, Rosemont, IL), 1:2000 rabbit anti-human PEX5, PEX6 (gifts from Dr. Gabriele Dodt, University of Tübingen), 1:17000 rabbit anti-human β-tubulin (Abcam, ab6046, Cambridge, MA), followed by appropriate HRP-conjugated secondary antibodies, and visualized by ECL using an Amersham 600 platform. Band quantification (densitometry) was done using ImageJ (NIH).

2.6.2. Primary fibroblasts were seeded onto coverslips in 12-well plates and prepared for indirect immunofluorescence as previously described (Slawecki et al., 1995)

Primary antibodies:1:400 rabbit anti-human PEX5 (gift from Gabriele Dodt, University of Tübingen); 1:400 sheep anti-human ABCD3 (gift from Steven Gould, Johns Hopkins University); secondary antibodies: 1:400 anti-rabbit 488 (Invitrogen, Waltham, MA), 1:300 anti-sheep Texas Red (Sigma-Aldrich). Slides were visualized using an Olympus BX51 microscope (Center Valley, PA) at 60x magnification; images were captured using an Olympus CCD camera and MagnaFire software (Olympus, Center Valley, PA).

2.7. Retinal histology and immunohistochemistry

2.7.1. Retinal histology was performed as previously described (Polosa et al., 2017)

Briefly, following overnight fixation in 4% paraformaldehyde, eyes were embedded in Epon resin. 1 μm sections cut at the level of the optic nerve head were collected on glass slides and stained with 0.1% toluidine blue. Samples were visualized using a Zeiss CZC0M0042 microscope and images captured using a Zeiss AxioCam MRc camera. Thickness of retinal layers was measured using AxioVision software (version 4.8.2.0; Carl Zeiss Microscopy GmbH). 5–15 measurements from across each retinal section were used to calculate mean layer

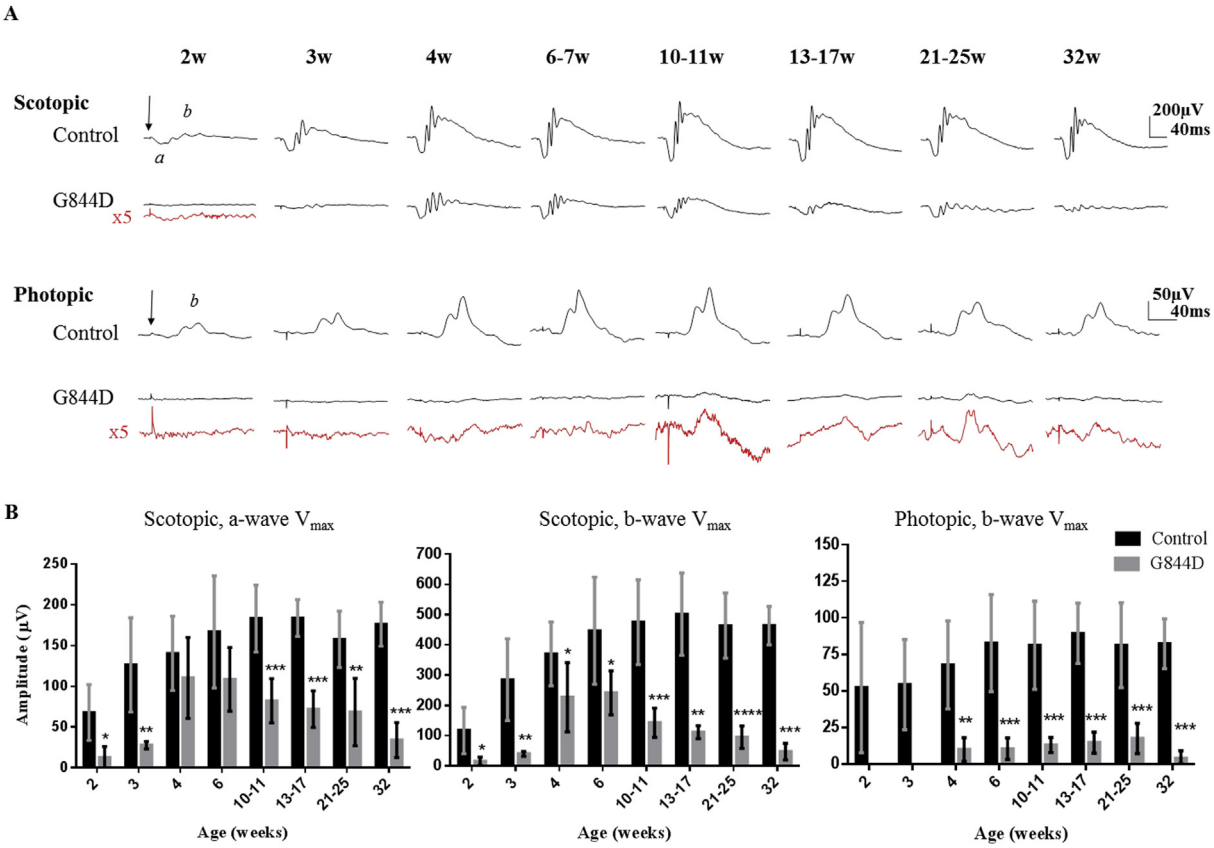

Figure 1. ffERG maturation in PEX1-G844D mice. (A) Representative waveforms show diminished scotopic and photopic retinal electrophysiological responses in PEX1-G844D homozygous mice compared to controls from 2 to 32 wks of age. In PEX1-G844D mouse waveforms, red tracings represent 5-fold amplification of the original scotopic or photopic response in black to facilitate visualizing the low responses. **(B)** Quantification of maximum ffERG response shows that scotopic a- and b-wave amplitudes peak at 4–6 wks in PEX1-G844D mice then gradually diminish, while photopic b-waves remain consistently low. B-waves are affected earlier and more severely than a-waves. In a subset of cases, the same animal was tested at more than one time point. Error bars indicate standard deviation; Student's t-test * = $p < 0.05$, ** = $p < 0.01$, *** = $p < 0.001$; n = 4–7 per group.

values.

2.7.2. For immunohistochemistry eye cups were fixed 3 h in 4% paraformaldehyde, incubated in 10% (30 min on ice), 20% (1 h on ice), and 30% (4 °C overnight) sucrose in 0.1M PB, then embedded and frozen in frozen section compound (VWR, Radnor, PA)

5 µm retinal cryo-sections were blocked (1% NGS, 0.1% Triton, 10% BSA in PBS) for 1 h, washed, incubated at 4 °C overnight with primary antibody in incubation buffer (0.1% Triton, 10% BSA in PBS), washed, incubated 90 min with secondary antibody and washed. Coverslips were mounted using ProLong Gold antifade reagent with DAPI (Invitrogen, Carlsbad, CA) and retinas were visualized using a Leica DMI600 microscope with DFC345FX camera and LASX software (Richmond Hill, Canada). Primary antibodies used were 1:450 rabbit anti-human PEX1 (Proteintech 13669-1-AP, Rosemont, IL), 1:50 goat anti-human PEX6 (Abcam ab175064, Cambridge, MA), 1:300 rabbit anti-human PEX14 (gift from Paul Watkins, Johns Hopkins University), 1:200 rabbit anti-human glial fibrillary acidic protein (Sigma G9269, St. Louis, MO), 1:200 rabbit anti-human calbindin D-28K (Sigma C9848, St. Louis, MO), 1:300 mouse anti-human rhodopsin (Phosphosolutions 1840-RHO, Aurora, CO), 1:200 rabbit anti-human synaptophysin (Abcam ab14692, Cambridge, MA), 1:300 rabbit anti-human cone arrestin (Millipore AB15282, Burlington, MA), 1:150 mouse anti-human glutamine synthetase (Millipore MAB302, Burlington, MA), 1:300 rabbit anti-human PKC-α (Abcam ab32376, Cambridge, MA), 1:200 rabbit anti-human parvalbumin (Abcam ab11427, Cambridge, MA). Secondary antibodies used: 1:400 anti-rabbit 488 (Jackson ImmunoResearch Laboratories 711-095-152, West Grove, PA),1:300 anti-goat Texas Red (Invitrogen PA1-28662, Carlsbad, CA), 1:300 anti-mouse Texas Red (Invitrogen T-862), 1:100 anti-mouse 488 (Invitrogen A32723, Carlsbad, CA).

2.8. Transmission electron microscopy

Mice were perfused with 0.1M sodium cacodylate buffer (Electron Microscopy Sciences, EMS, Hatfield, PA) containing 0.1% calcium chloride (Bioshop, Burlington, Canada), 2.5% glutaraldehyde (EMS, Hatfield, PA), 2% paraformaldehyde (Fisher, Hampton, NH). Eyes were fixed in 2.5% glutaraldehyde in 0.1M sodium cacodylate buffer for 1 h; lenses were removed and eye cups quartered, washed and post stained with 1% osmium + 1.5% potassium ferrocyanide (both EMS, Hatfield, PA), dehydrated by increasing concentrations of acetone (Fisher Scientific, Ottawa, Canada), infiltrated with increasing concentrations of Epon (EMS, Hatfield, PA), then polymerized with pure Epon at 60 °C for 48 h. 100 nm sections were cut with a Leica UCT ultramicrotome (Wetzlar, Germany), placed onto a 200 mesh copper grid, post stained with uranyl acetate and Reynold's lead, and imaged with the FEI Tecnai 12 BioTwin TEM (Hillsboro, OR) equipped with the AMT XR80C CCD camera at an accelerating voltage of 120 kV.

Mitochondria size on electron microscopy images was determined by manually tracing around each individual mitochondrion and using ImageJ software (NIH, Bethesda, MD) to calculate its area. 8–36 mitochondria were measured per animal for a total of 37 mutant and 79 control mitochondria scored from 3 mice of each genotype.

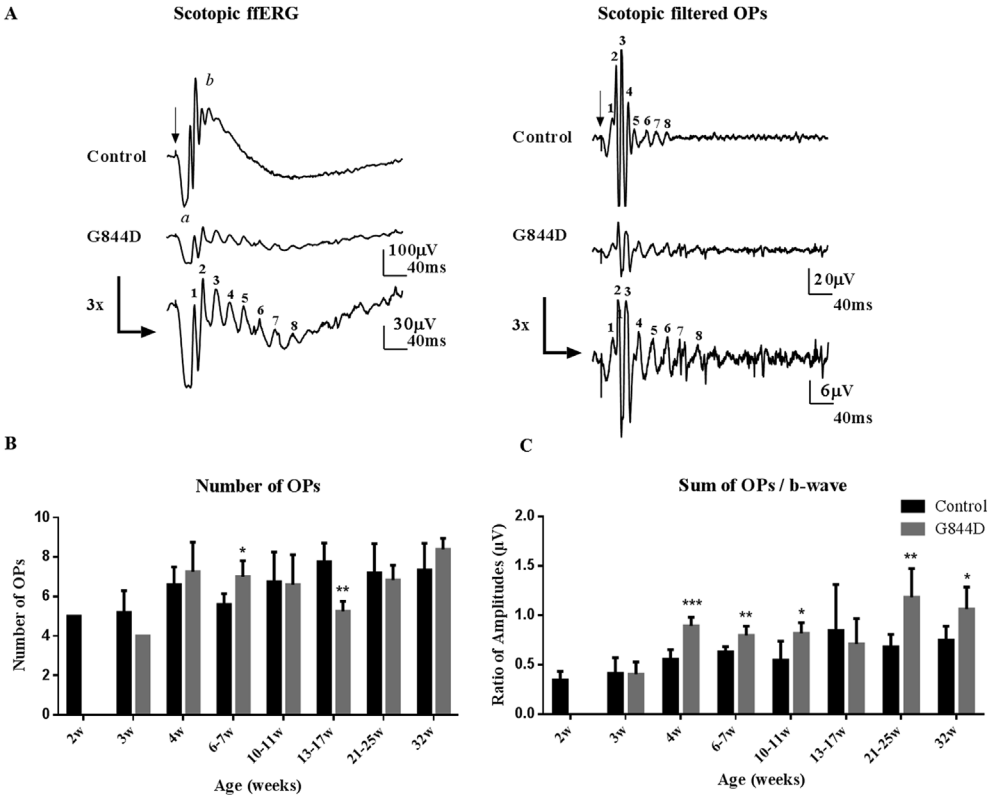

Fig. 2. Prominence of oscillatory potentials (OPs) in ffERGs of PEX1-G844D mice. (A) Representative waveforms taken at 32 wks of age show that OPs are preserved in PEX1-G844D mice, despite diminished a- and b-wave amplitude. On the left are the original ffERG waveforms (bandwidth: 1–1000Hz) with all ERG components, and on the right are the same waveforms filtered (bandwidth: 100–1000Hz) to highlight the OPs. **(B)** The total number of OPs on the ascending and descending scotopic waveform is presented at each age. OPs in PEX1-G844D mice were first recognizable at 3 wks of age, and then followed a similar maturation pattern as controls. A significant difference in OP number between mutants and controls occurred only at 6–7 weeks and 13–17 wks, though one genotype was not consistently higher or lower than the other. **(C)** To compare the OP preservation relative to the b-wave amplitude, the sum of OP amplitudes in each waveform was divided by the respective b-wave amplitude. This ratio was significantly higher in PEX1-G844D mice compared to controls starting at 4 wks, with the exception of the 13–17 wk age group. Error bars indicate standard deviation; Student's t-test * = $p < 0.05$, *** = $p < 0.001$; n = 4–7 per group.

2.9. Statistical analysis

N = 4–7 at each age and genotype for ffERG, n = 5 for VEP, n = 7–13 for OKR, N = 3–4 for all structural/histological analyses, n = 3 for protein levels and fibroblast studies, and n = 13–17 for biochemical analyses. For all quantitative measures, PEX1-G844D data were compared for statistical significance ($p < 0.05$) using an unpaired two-tailed student's t-test. Both male and female mice were used in equal numbers, and no sex-related difference was observed.

3. Results

3.1. Assessing retinal function

3.1.1. Scotopic (rod-mediated) response

Representative scotopic and photopic ffERG waveforms evoked by flashes of light at 0.9 log cd.s.m^{-2} luminous intensity are shown in Fig. 1A, and amplitude quantification shown in Fig. 1B. In control mice, scotopic ffERG recorded at the time of eye opening (2 wks of age) presented a waveform with easily identifiable a- and b-waves (68 ± 34 μV and 117 ± 76 μV, respectively). These parameters increased significantly in amplitude with age to reach maximum values between 13 and 17 wks of age (184 ± 23 μV, 501 ± 136 μV, a- and b-waves, respectively; unpaired *t*-test, $p < 0.005$), representing an increase of 2.7-fold (a-wave) and 4.3-fold (b-wave) over the 2-wk values. No significant differences were observed with further aging to 32 wks.

In PEX1-G844D mice, the scotopic response recorded at 2 wks of age required enhanced amplification to be visible (represented by red tracing below original response in black, Fig. 1A). The amplitudes of the a- and b-waves (16 ± 9 μV and 20 ± 7 μV, respectively), were only 24% and 17% of average age-controlled values. Amplitudes significantly increased with age, peaking at 6 weeks (108 ± 39 μV and 241 ± 73 μV, a- and b-waves, respectively; unpaired *t*-test, $p = 0.007$ and $p = 0.002$), representing a 6.8-fold (a-wave) and 12.1-fold (b-wave) increase. From 6 to 32 wks, retinal function gradually declined, reaching 34 ± 21 μV (a-wave) and 47 ± 27 μV (b-wave) or 69% and 80% of peak values, respectively (unpaired *t*-test, $p = 0.02$). These values represent 19% and 10% of age-matched control values at 32 wks of age. With the exception of the a-wave amplitude at 4 and 6 wks, a- and b-waves were significantly reduced at all ages in mutants compared to controls (*t*-test, $p < 0.05$–0.001, Fig. 1B).

Peak latency data is presented in Supplemental Fig. 1. Scotopic, a-wave peak times were delayed only in the 13–17 wk and 32 wk age groups by 5 ms and 10 ms respectively (unpaired *t*-test, $p = 0.04$ and $p = 0.0006$). Scotopic b-wave peak times were delayed from 4 to 32 wks by an average of 24 ms–40 ms (unpaired *t*-test, $p = 0.03$ to $p < 0.001$).

3.1.2. Photopic (cone-mediated) response

Photopic ffERG responses were clearly detectable in control mice at 2 wks of age and had a mean b-wave amplitude of 26 ± 15 μV (Fig. 1A and B). Values peaked between 13 and 17 wks of age (89 ± 21 μV) and this increase was statistically significant (unpaired *t*-test, $p = 0.005$), and remained consistent to 32 wks of age (unpaired *t*-test, $p = 0.61$).

In contrast, a reproducible photopic response could not be detected in PEX1-G844D mice until they reached 4 wks of age. At this age, the average photopic amplitude (10 ± 8 μV) was 15% that of controls, and remained significantly lower than normal until 32 wks, never surpassing 22% of normal, which occurred at 21–25 wks (unpaired *t*-test, $p < 0.01$–0.001, Fig. 1B). There was no latency difference in photopic conditions, irrespective of age (Supplemental Fig. 1).

3.1.3. Oscillatory potentials

Despite a marked b-wave amplitude decline in PEX1-G844D mice, the OPs remained prominent features of the scotopic ffERG waveform, as illustrated in Fig. 1A and better evidenced in Fig. 2A, which represents a waveform taken at 32 wks of age. The number of OPs at each age is presented in Fig. 2B. By 2 wks of age, 5 ± 0 clearly identifiable scotopic OPs shaped the ascending and descending limbs of the b-wave in control mice. In controls, the average number of OPs increased

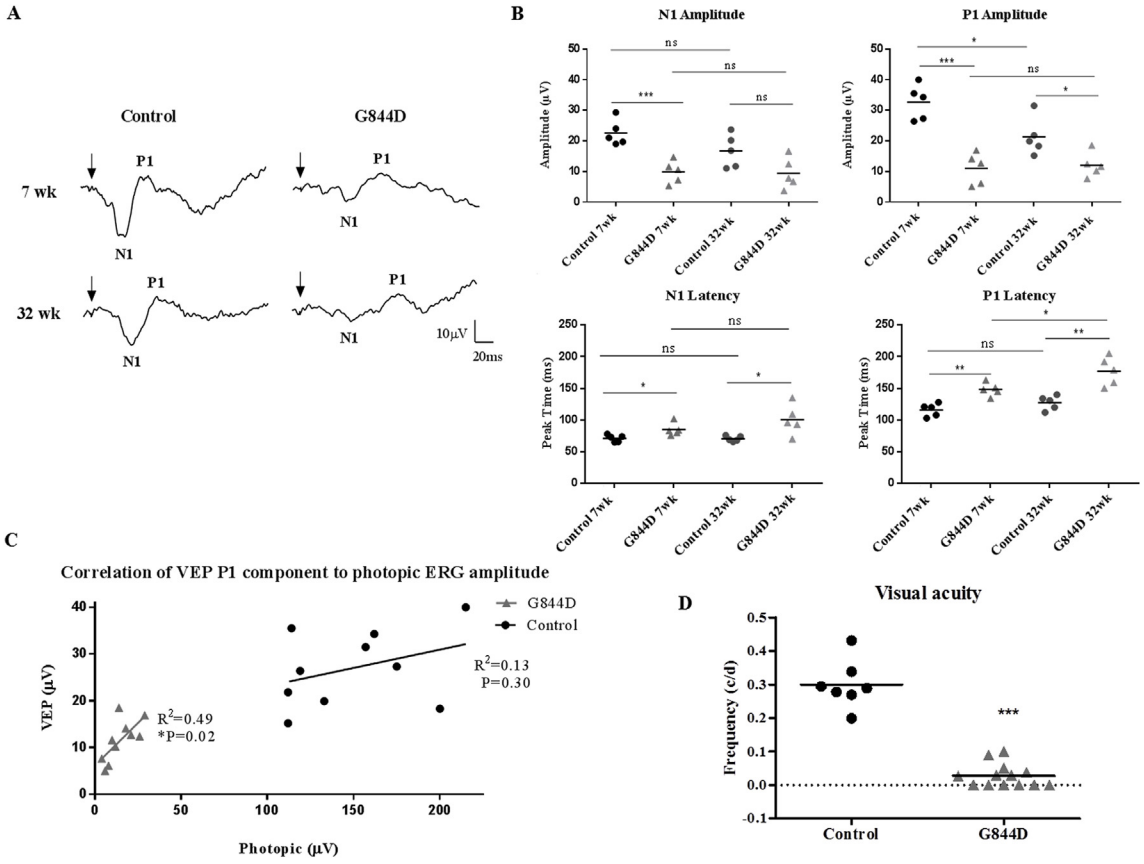

Fig. 3. Visual evoked potential (VEP) and visual acuity in PEX1-G844D mice. (A) Representative photopic VEP waveforms show decreased but variable VEP N1 and P1 deflections at 7 and 32 wks. Different animals were tested at each time point. **(B)** Quantification of photopic VEP waveforms shows diminished N1 and P1 amplitudes and increased latency in PEX1-G844D mice. Although diminished, N1 and P1 amplitude of PEX1-G844D mice remained consistent from 7 to 32 wks, while in controls P1 decreased with age. In the mutants P1 latency increased with age but remained consistent in controls. **(C)** VEP amplitude is positively correlated to photopic ffERG b-wave amplitude in PEX1-G844D mice (linear regression analysis, P = 0.02). **(D)** Visual acuity was measured by determining the spatial frequency threshold of the optomotor reflex. Visual acuity was severely diminished in PEX1-G844D mice at 11–13 weeks of age. Each mouse was tested twice and the average visual acuity from both eyes per test was taken. Each point represents 1 animal; Student's t-test * = $p < 0.05$, ** = $p < 0.01$, *** = $p < 0.001$, ns = not statistically significant.

significantly to 7 ± 1 OPs (unpaired *t*-test, p = 0.01) at 4 wks and remained at that level throughout (7 ± 1 OPs; unpaired *t*-test, p = 0.01 at age 32 weeks). In PEX1-G844D mice, OPs were first recognizable at 3 wks of age (4 ± 0 OPs). The mutants followed a similar maturation pattern to controls, with the average number of OPs rising to 7 ± 2 OPs (unpaired *t*-test, p = 0.005) at 4 wks. The average number of OPs reached 8 ± 1 by 32 wks, but this was not significantly different from 4 wks (unpaired *t*-test, p = 0.62). Comparing controls to mutants, a significant difference in OP number occurred only at 6–7 weeks (6 ± 1 vs 7 ± 1, respectively, unpaired *t*-test, p = 0.02) and 13–17 weeks (8 ± 1 vs 5 ± 1, respectively, unpaired *t*-test, p = 0.004). However, one genotype was not consistently higher or lower than the other. To compare the OP preservation relative to the b-wave amplitude and to see if one of these parameters was more or less affected in our model, the sum of OP amplitudes in each waveform was divided by the respective b-wave amplitude (Fig. 2C). This ratio was significantly higher in PEX1-G844D mice compared to controls starting at age 4 wks, with the exception of the 13–17 wk age group (unpaired *t*-test, p < 0.05–0.001), suggesting a relative preservation of OP compared to b-wave amplitude.

3.2. Assessing the primary visual pathway (from the retina to the visual cortex)

Representative visual evoked potential (VEP) recorded from control and PEX1-G844D mice at 7 and 32 wks of age are shown in Fig. 3A. A typical VEP waveform in control mice was composed of a negative waveform (N1) and a more prominent positive waveform (P1). In mutant mice, these two components were present but of lower amplitude. In PEX1-G844D mice, the N1 amplitude was on average 44% of that of littermate controls at 7 wks (99 ± 37 μV versus 226 ± 42 μV, unpaired *t*-test p = 0.0009) (Fig. 3B). At 32 wks of age the average N1 amplitude was 94 ± 51 μV and 167 ± 55 μV in mutants and controls, respectively, but this difference was not statistically significant. The N1 peak time at 7 wks was delayed by 14 ms on average in mutants compared to controls (85 ± 10 ms versus 71 ± 6 ms; unpaired *t*-test p = 0.027) and delayed by 29 ms at 32 wks (101 ± 24 ms versus 71 ± 4 ms; unpaired *t*-test, p = 0.024). However, the difference in latency between the younger and older PEX1-G844D cohorts was not statistically significant. P1 amplitude in PEX1-G844D mice was on average 34% that of age-matched controls at 7 wks (110 ± 52 μV versus 327 ± 58 μV; unpaired *t*-test, p = 0.0002), and 57% that of age-matched controls at 32 wks (121 ± 40 μV versus 213 ± 62 μV; unpaired *t*-test, p = 0.023) (Fig. 3B). Although the average P1 amplitude in control mice was lower in the older compared to younger age group (213 ± 62 μV versus 327 ± 58 μV, respectively; unpaired *t*-test, p = 0.017), there was no significant difference among age groups in PEX1-G844D mice (110 ± 52 μV versus 121 ± 40 μV). In the mutants, the average P1 peak time at 7 wks was 148 ± 10 ms, delayed by an average of 32 ms from the average control peak time of 116 ± 10 ms (unpaired *t*-test, p = 0.0012). This delay significantly increased to 50 ms (unpaired *t*-test, p = 0.0329) in the 32-wk old mice, when

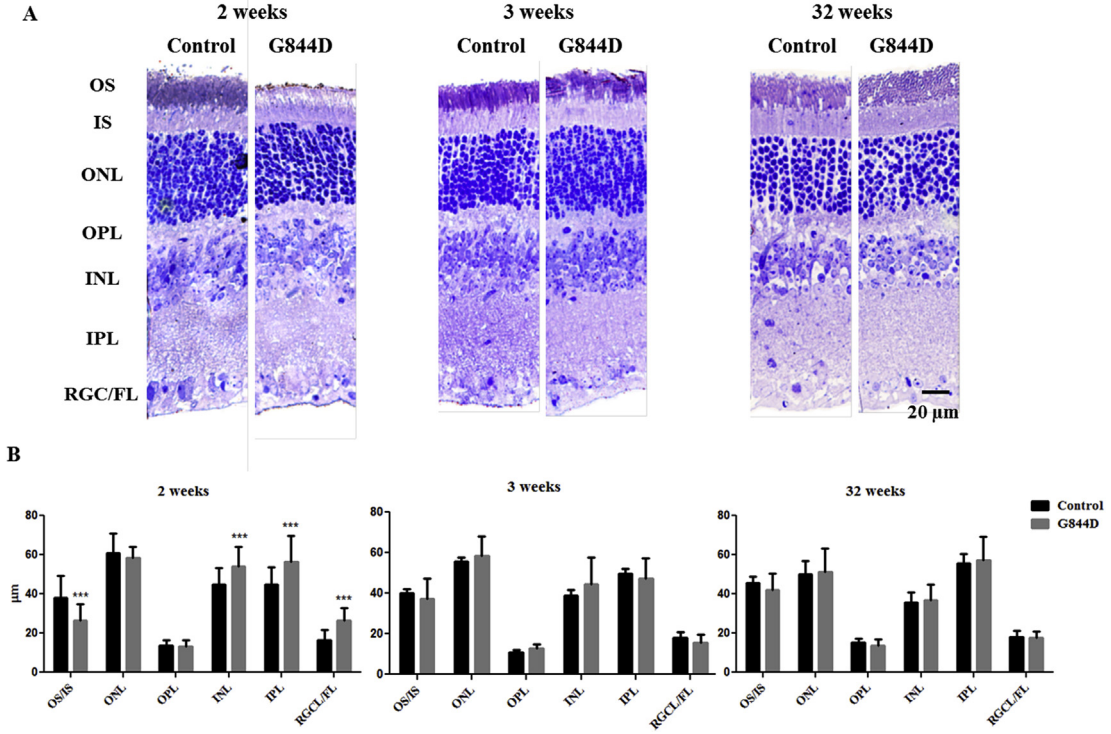

Fig. 4. Retinal histology shows preservation of retinal layers and thickness in PEX1-G844D mice after 2 wks of age. (A) Retinal sections stained with Toluidine blue show preserved retinal layers in PEX1-G844D retinas compared to controls. **(B)** Quantitative measures of retinal cell layers at 2, 3, and 32 wks of age show shortened OS thickness, and increased INL, IPL, and RGC/FL thickness in PEX1-G844D mice compared to controls at 2 wks of age. These differences disappear by 3 wks of age and remain consistent to 32 wks. Sections were taken near the central retina and measurements taken at various locations across the length of each section. Samples were assessed at 2, 3, 6, 10, and 32 wks, with representative images and plots shown at 2, 3 and 32 weeks. Student's t-test, *** = $p < 0.001$. (For interpretation of the references to colour in this figure legend, the reader is referred to the Web version of this article.)

mutants had a peak time of 177 ± 23 ms, compared to the control average of 127 ± 11 ms (unpaired *t*-test, $p = 0.0024$).

Although delayed, VEP amplitude directly correlated to photopic ffERG b-wave amplitude in PEX1-G844D mice (Fig. 3C, $R^2 = 0.49$, $p = 0.02$). That is, the higher the photopic ffERG response, the greater the VEP amplitude, and vice versa. There was no correlation between the VEP N1 and photopic ffERG amplitudes (not shown). In controls, however, the VEP amplitudes were more variable, and did not correlate to the photopic ffERG response (Fig. 3C, $R^2 = 0.13$, $p = 0.30$).

Visual acuity was measured by determining the spatial frequency threshold of the optomotor reflex at 11–13 wks of age (Fig. 3D). In controls, the average spatial frequency threshold was 0.3 ± 0.07 cycles/degree (c/d). In PEX1-G844D mice, this value was diminished to 0.03 ± 0.03 c/d, on average one tenth that of control (unpaired *t*-test, $p < 0.001$). This observation supports the reduced ffERG and VEP measures, which were also performed in photopic conditions. That is, attenuated retinal response results in reduced signal transmission, and thus lower functional vision.

3.3. Retinal structure

3.3.1. Histology

To better understand the pathophysiology of retinal dysfunction in PEX1-G844D mice, histology with toluidine blue staining was performed to identify any structural defects from early to advanced age (Fig. 4A). At 2 wks of age, all the retinal layers were present in the mutants. The retinal outer segment/inner segment layer (OS/IS) was on average 11 µm thinner in mutants than controls (27 ± 8 µm in mutants versus 38 ± 11 µm in controls, unpaired *t*-test, $p < 0.001$, Fig. 4B), but there was no significant difference in outer nuclear layer (ONL) or outer plexiform layer (OPL) thickness. In contrast, the inner nuclear layer (INL) (54 ± 10 µm and 45 ± 8 µm), inner plexiform layer (IPL) (56 ± 13 µm and 45 ± 9 µm), and retinal ganglion cell/fibre layer (RGC/FL) (26 ± 7 µm and 16 ± 5 µm), were significantly thicker in PEX1-G844D mice compared to controls (unpaired *t*-test, $p < 0.001$). However, by 3 wks of age there was no difference in retinal layer thickness between mutants and controls (Fig. 4B), and this remained consistent to 32 wks (Fig. 4A and B). Retinal morphology was also assessed at 6 and 10 wks of age and no differences were found (not shown).

3.3.2. Immunohistochemistry

As no major histological changes were observed using light microscopy and toluidine blue staining, immunohistochemistry was then performed to detect more subtle histological changes affecting specific cell types. As seen in Fig. 5, PEX1-G844D retinas exhibited normal immunoreactivity for markers of rod cell outer segments (rhodopsin), horizontal cells (calbindin), amacrine cells (parvalbumin), Müller cells (glutamine synthetase), and all synaptic layers (synaptophysin) when compared to controls. This observation was consistent from 6 to 32 wks.

In contrast, immunoreactivity against cone arrestin, which specifically binds to cone cells from the OS to the synaptic terminal, revealed an altered cone structure in PEX1-G844D mice (Fig. 6A). In addition to diminished arrestin, most of the cone OS and IS components were absent, disorganized, or disrupted. There was a drastic synaptic retraction of cone axons and pedicles (at the OPL), resulting in an almost complete

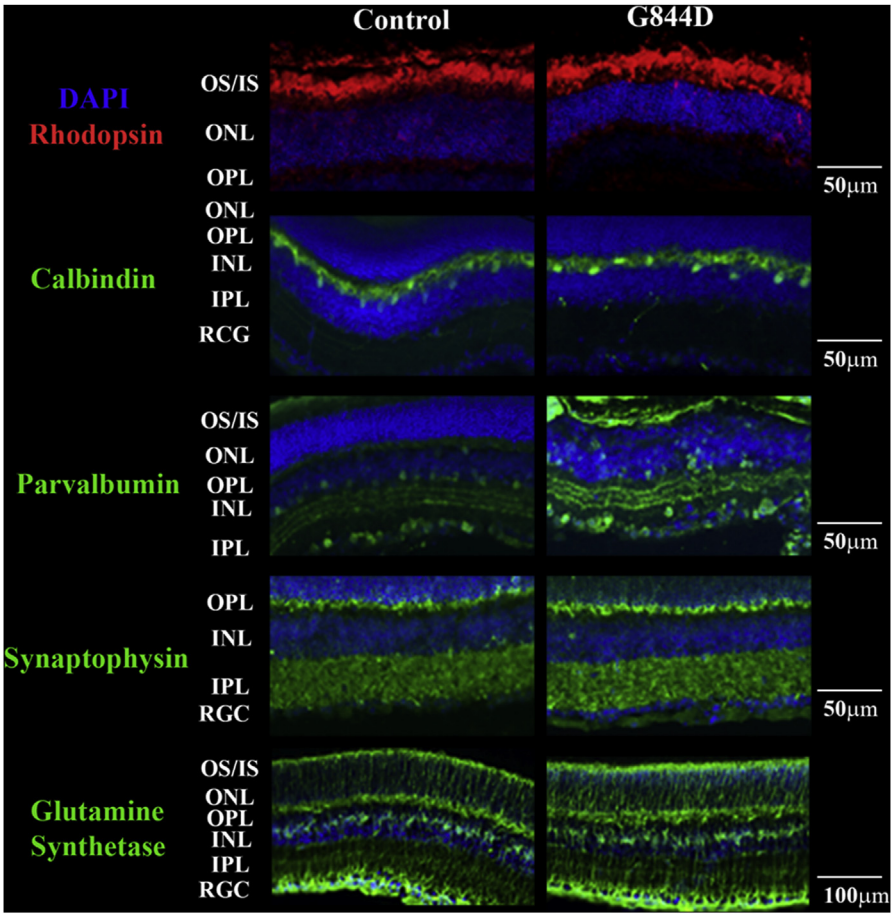

Fig. 5. Immunohistochemistry shows preservation of various cell structures in PEX1-G844D retinas. Retinal immunohistochemistry reveals normal immunoreactivity of the rod cell outer segment (rhodopsin), amacrine cells (parvalbumin), horizontal cells (calbindin), Müller cells (glutamine synthetase), and synaptic layers (synaptophysin) in PEX1-G844D mice compared to littermate controls. Retinas were assessed at 6, 13, and 32 wks of age and representative images shown (n = 3).

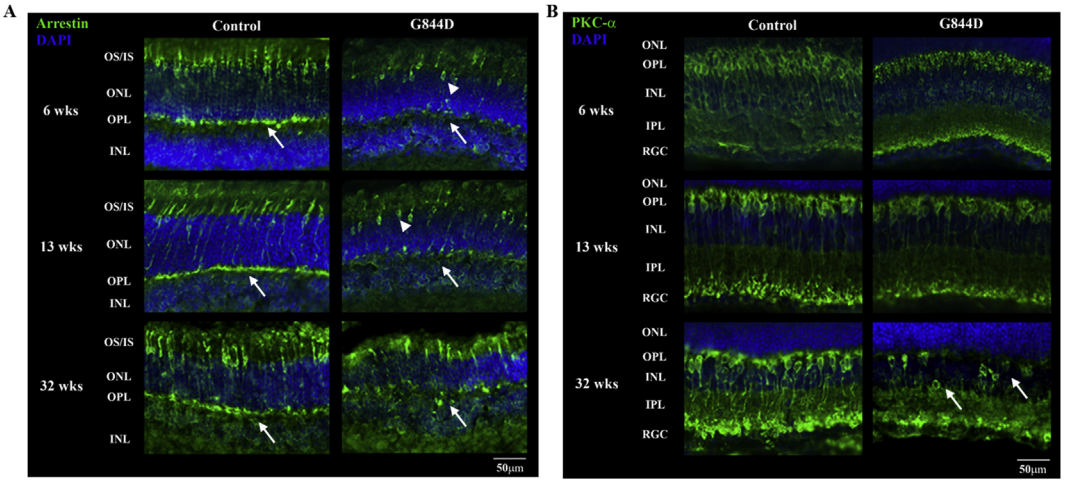

Fig. 6. Immunohistochemistry shows decreased cone and bipolar cells in PEX1-G844D retinas. (A) Cone arrestin is decreased from 6 to 32 wks in PEX1-G844D mice compared to littermate controls, especially visible when viewing the cone cell synapses at the OPL (white arrows). Most cone cells had absent OS and IS components, and apparent loss of contact with the INL cells (synapses, white arrows). Some cells had staining of their nuclei only (white arrowhead). **(B)** ON bipolar cells (PKC-α) were present at normal numbers at 6 and 13 wks, but diminished and displaced (white arrows) into the IPL by 32 weeks in PEX1-G844D mice compared to littermate controls. Connections between photoreceptors and bipolar cells (OPL) and connections to the RGC layer were reduced. Representative images are shown at each age point (n = 3).

loss of contact with the INL cells with some cone photoreceptors only exhibiting staining of their nucleus. These morphological alterations were observed at 6 wks of age, the earliest time point tested, and remained similar to 32 wks of age. Comparable changes were observed in the rod ON bipolar cells, which were visualized using antibodies against protein kinase C alpha (PKC-α). Although PKC-α immunoreactivity was relatively normal at 6 and 13 wks of age in the mutants, by 32 wks fewer ON rod bipolar cells were detected compared to controls (Fig. 6B). Some of these remaining cells migrated towards the center of the inner plexiform layer (IPL) (Fig. 6B; white arrows). In addition, both bipolar cell dendritic terminals (which establish connections with rod spherules in the OPL) and bipolar end-bulb axon terminals (which extend into the IPL connecting with RGCs), were significantly reduced. Finally, immunolabelling for Glial Fibrillary Acidic Protein (GFAP), a

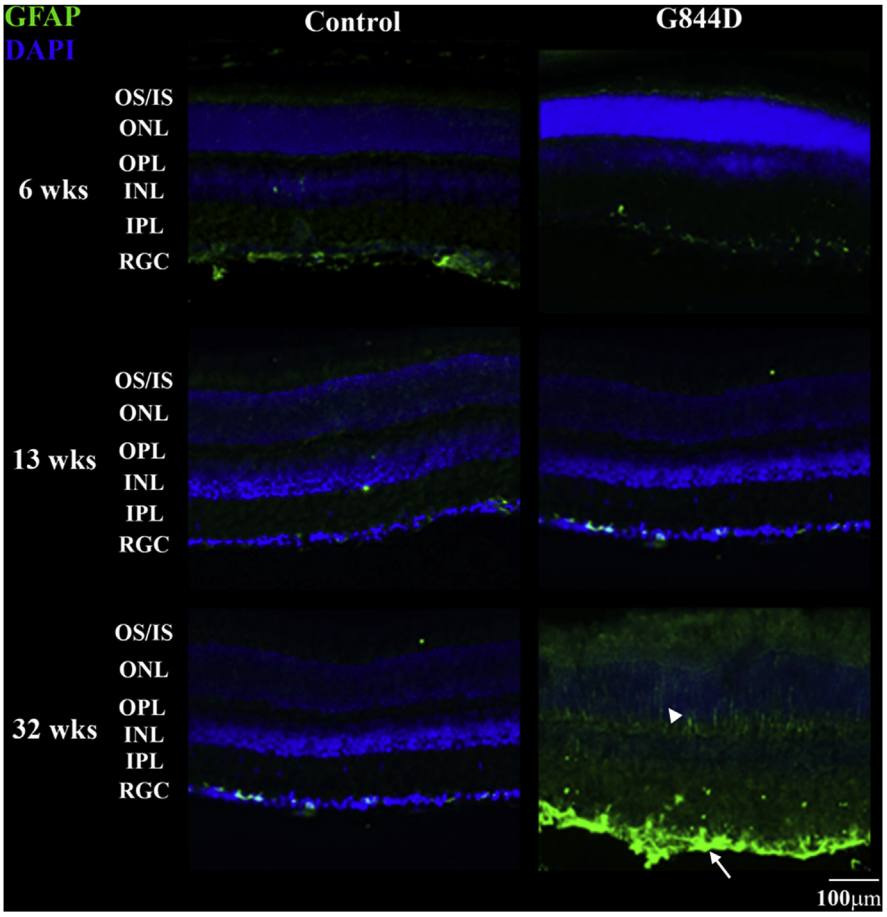

Fig. 7. Prominence of glial fibrillary acidic protein with age in PEX1-G844D retinas. Retinal immunohistochemistry against GFAP is strongly apparent by 32 wks in PEX1-G844D retinas in Müller cell radial processes (white arrowhead) and RGC astrocytes (white arrow) but not in littermate controls. Representative images shown (n = 3).

gliosis marker expressed by astrocytes (in the RGC layer) and activated Müller cells, was increased in PEX1-G844D retinas only at 32 wks of age (Fig. 7), suggesting Müller cell activation. Little to no GFAP immunoreactivity was evidenced in controls and mutants at 6 or 13 wks of age, and limited to the RGC (astrocyte and Müller endfeet).

3.3.3. Transmission electron microscopy

Transmission electron microscopy was used to visualise retinal ultrastructure from 32-wk-old PEX1-G844D and control mice. Photoreceptor OS appeared to have normal density and disc membrane organization (Fig. 8A). However, there was no linearly aligned IS structure in the mutants, in contrast to the organized IS seen in controls (Fig. 8B). This could imply that the mutant IS were either disorganized or degenerated to the point of non-detection by our method. In addition, mitochondria were enlarged on average 3-fold throughout PEX1-G844D retinas compared to those in controls (0.41 ± 0.39 units in mutants versus 0.14 ± 0.10 units in controls, unpaired *t*-test, $p < 0.001$), particularly remarkable in the mitochondria-rich IS (Fig. 8C). Mitochondrial size was measured using ImageJ and a total of 37 mutant and 79 control mitochondria scored from 3 mice of each genotype (data not shown). No other defects were visible in the remaining cellular layers (Supplemental Fig. 2).

3.4. Peroxisome protein and biochemical metabolite levels

3.4.1. Peroxisome protein levels

Immunoblotting was performed to compare the amounts of PEX1-G844D to wild-type PEX1 in the retina. There were normal amounts of PEX1-G844D, its binding partner PEX6, and its putative ligand PEX5 (the peroxisome enzyme receptor) protein in mutant compared to control retinas, suggesting that the mutated protein is not degraded (Fig. 9A). Protein amounts were compared using band densitometry normalized to the loading control (not shown). This was consistent from 7 to 32 wks of age and in all other tissues tested (including fibroblasts, liver, kidney, spleen, brain; not shown). Immunohistochemistry showed localization of PEX1-G844D and PEX6 at the photoreceptor inner segment and outer plexiform layer, similar to their localization in control mice (Fig. 9B), with slightly lower PEX1-G844D at the OPL. The peroxisome membrane protein PEX14, enriched at the inner segment, was also normally localized in PEX1-G844D retinas through 32 wks.

3.4.2. PEX1 function

In light of normal PEX1-G844D protein levels and localization, the protein's function to remove PEX5 from the peroxisomal membrane was assessed using immunofluorescent microscopy on primary mouse fibroblasts (Fig. 9C). In control cells, PEX5 is primarily cytosolic, but in PEX1-G844D cells it co-localized with the peroxisome membrane protein ABCD3, indicating peroxisomal accumulation. Taken together, inefficient PEX5 recycling despite normal PEX1-G844D protein levels indicates that the missense protein is subfunctional.

3.4.3. Peroxisome metabolites

PEX mutations disrupt peroxisome metabolism, resulting in an accumulation or deficiency in the biochemical metabolites of these pathways. The affected pathways and extent of these effects vary by tissue. Two well-known peroxisome-mediated processes are very long-chain fatty acid (VLCFA) β-oxidation and plasmalogen synthesis (Wanders and Waterham, 2006). Disruption in these pathways results in increased C26:0 VLCFA and decreased plasmalogens, and these metabolites are commonly measured in the blood for ZSD diagnosis, though can be normal in milder cases (Ratbi et al., 2015; Braverman et al., 2016). In retinas from 4wk to 32 wk old PEX1-G844D mice, C26:0

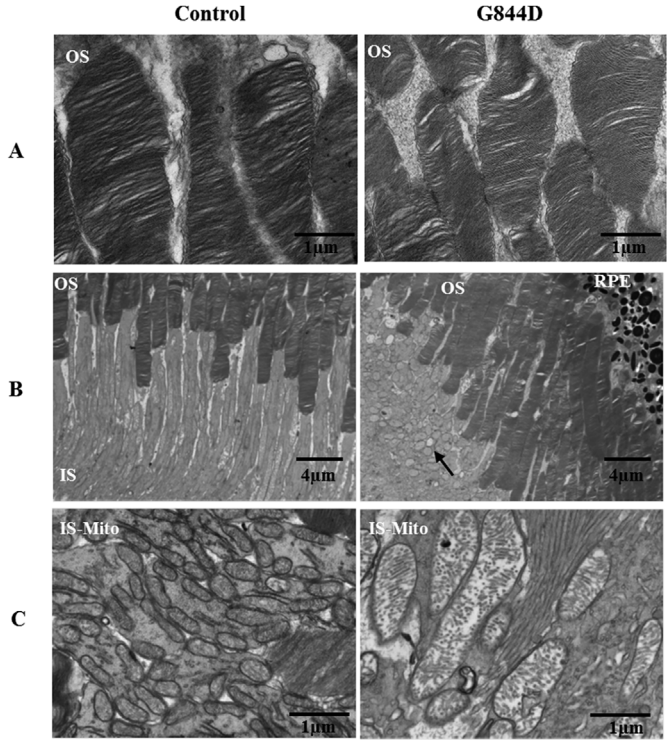

Fig. 8. Transmission electron microscopy of PEX1-G844D retinas. (A) Photoreceptor outer segments had normal density and opsin organization (11,000x magnification). **(B)** Photoreceptor connections from outer to inner segments were disorganized in the mutants (1900x magnification). **(C)** Mitochondria were enlarged on average 3-fold throughout PEX1-G844D retinas, particularly evident in the mitochondria-rich inner segment (11,000x magnification). Findings were consistent in 3 mutant and 3 control retinas analyzed from 32-wk-old animals. Images of additional layers can be viewed in Supplemental Fig. 2.

VLCFAs (measured as C26:0 lyso-PCs) were elevated on average 5.8-fold compared to average wild-type control levels (1 ± 0.6 units in control versus 5.8 ± 5.1 units in mutants, unpaired *t*-test, p = 0.002). These values were, however, highly variable and ranged from normal to 18 times wild-type levels (Fig. 9D). Total phosphoethanolamine (PE) plasmalogen levels in PEX1-G844D retinas matched wild-type controls (1 ± 0.3 units in control versus 0.9 ± 0.5 units in mutants, unpaired *t*-test, p = 0.72) (Fig. 9D). Levels of individual PE-plasmalogen subspecies (sn1- C16:0, C18:0, C18:1, and sn2- 16:1, 18:0, 18:1, 20:4, 22:4 22:6) measured were also no different from control (not shown).

3.5. Discussion

The PEX1-G844D mouse model for mild ZSD exhibits an early onset cone deficit and progressive degeneration of rod function, with functional impairment precluding some cellular events, primarily ON bipolar cell loss. Although anatomical findings suggest the most important structural defect is at the photoreceptor level, with disruption at the inner retina occurring later, early scotopic electrophysiological observations suggest a greater inner retinal anomaly. This could indicate a functional deficiency despite apparently normal structure, as discussed further below.

3.5.1. Visual function and retinal architecture

The retinal electrophysiological response in PEX1-G844D mice was delayed in reaching maximal amplitude compared to controls and was near the threshold of detection (baseline noise level) until 3–4 wks of age (Fig. 1A and B). This lag followed by rapid improvement in retinal function correlates with the shortened OS/IS and thicker inner retina seen at 2 wks, which normalize by 3 wks (Fig. 4A and B). Throughout life, the scotopic ffERG in PEX1-G844D mice was diminished, with a-waves relatively better preserved than b-waves (Fig. 1A and B). As a-wave generation results from OS hyperpolarization (Brown, 1968), this observation is consistent with the relatively preserved rod OS thickness and organization in our model (Figs. 4, 5, 8A, B). We hypothesize that residual peroxisome activity is sufficient to sustain OS formation and partial function, even at 32 wks when the ultrastructure of the IS is disorganized or degenerated (Fig. 8A). B-wave generation results from the transfer of signal from photoreceptors to the inner retina, and involves mainly activation of inner retinal cells such as bipolar cells (Miller and Dowling, 1970; Dick and Miller, 1978). Thus, it is also consistent that b-wave response declines with age in our model, correlating with the reduction in ON bipolar cells (Fig. 6B). Despite this decline, high frequency ERG components (OPs) are better preserved than low frequency ERG components (a- and b-waves) in PEX1-G844D mice (Fig. 2B). Although their exact source is still debated, OPs originate in the inner retina and are considered the result of a negative feedback of bipolar on amacrine cells (Heynen et al., 1985). Taken together, the OP prominence and normal parvalbumin distribution in our mutants suggest that amacrine cell function is preserved (Fig. 5). In addition, we observed better preserved scotopic than photopic response in PEX1-G844D mice, at least earlier in life, suggesting a greater impairment of the cone versus rod mediated retinal function. This is corroborated by immunohistochemistry, in which the rod OS remains intact in the mutants, while cones are diminished and structurally abnormal, even at an early age (Figs. 5 and 6A).

GFAP expression occurs commonly in degenerative retinopathies, and appears at an older age in our model (Fig. 7). Although GFAP expression has been associated with photoreceptor degeneration, Müller cell activation after injury, and/or increased oxidative stress (Bringmann et al., 2009; Bramall et al., 2010), we hypothesize its presence here is due to the latter, with peroxisome dysfunction leading to accumulated reactive oxygen species over time.

Visual acuity measured by optokinetic reflex was diminished by 11–13 wks in PEX1-G844D mice, which is unsurprising given their severe cone deficit (Figs. 3D and 6A). The positive correlation of VEP to photopic ffERG amplitude indicates preserved retinocortical function in the mutants (Fig. 3C). However, despite photopic ffERG values never surpassing 22% of normal, VEP amplitudes averaged over 35% and 60% of age-matched controls at 7 wks and 32 wks, respectively. This could imply that the cell types or pathways responsible for retinocortical transmission are better preserved than the retina in our model. In contrast, there was no correlation between VEP and ffERG in controls, most likely due to declining VEP P1 amplitudes with age in the presence of stable ffERGs. In addition, we observed delayed VEP peak time in our mutant mice, which is likely due to the underlying retinal dysfunction but could alternatively involve optic nerve pathology or a defect at the visual cortex level. Similar to our mouse model, a study of milder ZSD patients also reported delayed and/or prolonged latency in patients with retinitis pigmentosa and reduced visual acuity (Berendse et al., 2016). Of note, there are no reports of cortical blindness in mild ZSD patients.

Electron microscopy revealed enlarged mitochondria in PEX1-G844D retinas (Fig. 8C). Besides sharing fission proteins and membrane material (Mohanty and McBride, 2013), peroxisomes and mitochondria share signalling interplay, and coordinate several metabolic processes (Fransen et al., 2017). In the context of peroxisome dysfunction, mitochondria could secondarily be affected by altered lipid composition of their membranes and increased ROS exposure. Mitochondria with structural and functional abnormalities were observed in *Pex13* null mouse brains (Rahim et al., 2016), and in *Pex5* null mouse livers (Dirkx et al., 2005). In severe ZSD patients, myofibrillar and liver mitochondria exhibited ultrastructural and functional defects (Goldfischer et al., 1973; Salpietro et al., 2015). However, these patients and models represent a more severe ZSD disease than that of patients homozygous for

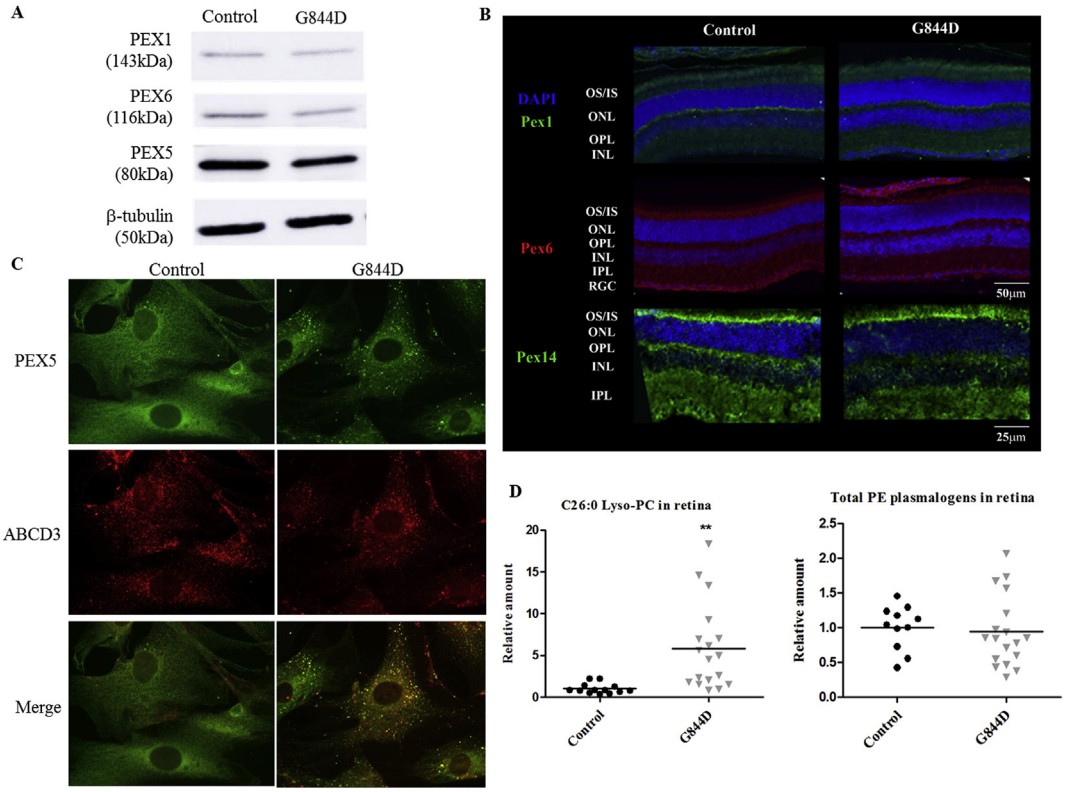

Fig. 9. Peroxisome protein and biochemical metabolite levels in PEX1-G844D retinas. (A) Immunoblotting of retinal lysates shows that PEX1-G844D protein is not degraded, and present at levels equal to that of wild-type PEX1 in controls. PEX6 and PEX5 levels are also normal. Both retinas from each mouse were pooled (n = 3), and representative image shown. **(B)** Immunohistochemistry showed normal localization of PEX1-G843D (primarily at the inner segment and outer plexiform layer), and PEX6 in the mutant compared to control retinas. **(C)** In control fibroblasts PEX5 is distributed throughout the cytosol, but in PEX1-G844D is primarily localized at peroxisomes. Images were visualized by indirect immunofluorescent microscopy with PEX5 (green) and peroxisome membrane protein ABCD3 (red); colocalization (yellow). Cell lines from 3 different mice and littermate controls were analyzed and representative images shown. **(D)** Levels of VLCFA (C26:0 lyso-PC) and ethanolamine (PE) plasmalogens were measured by LC/MSMS in mouse retinas. Average C26:0 lyso-PC levels were increased nearly six-fold compared to controls. Total PE plasmalogens levels were unchanged. Results from three separate experiments using 4wk and 32wk old mice were similar and pooled by normalizing all values against the control average for each experiment. Each point represents one whole retina; Student's two-tailed *t*-test, **p $<$ 0.01. (For interpretation of the references to colour in this figure legend, the reader is referred to the Web version of this article.)

PEX1-G843D or the PEX1-G844D mouse model. Nonetheless, secondary mitochondrial dysfunction has been observed in mice and humans with various non-etiologically related retinal degenerative diseases (Barot et al., 2011), and a possible mitochondrial contribution to PEX1-G844D mouse pathology warrants further study.

3.5.2. Peroxisome dysfunction and the retina

Protein levels of PEX1-G844D, its partner protein PEX6, and its ligand PEX5, are normal in the PEX1-G844D retina (Figure 9A). This is contrary to patient fibroblasts, in which PEX1-G843D protein amounts are degraded to 5–15% of normal PEX1 levels, with equivalent reductions in PEX6 (Walter et al., 2001; MacLean et al., 2019). Consequently, polyubiquitinated PEX5 accumulates at the peroxisome membrane and is degraded. We see a similar PEX5 accumulation at peroxisomes in PEX1-G844D mouse fibroblasts (Figure 9C), indicating the missense protein is subfunctional. It may be that the structure of mouse PEX1-G844D and the murine PEX1-PEX6 complex is more stable than its human counterpart, or that the murine protein degradation process is more tolerant of certain structural changes.

PEX1, PEX6, and PEX14 were found throughout control and PEX1-G844D retinas, as expected for peroxisomal biogenesis proteins, with PEX14 more concentrated at the inner segment (Figure 9B), and PEX1/PEX6 enriched at the inner segment and inner plexiform layer. This pattern corroborates that reported in normal mouse retina (Smith et al., 2016). Ultrastructural studies in normal mouse and human retina showed PEX6 concentrated at the OS/IS junction distal to the connecting cilia (Zaki et al., 2016). Peroxisome concentration in the IS could be required to support the continuous regeneration and high metabolic demand of the OS (Organisciak and Vaughan, 2010). Even so, peroxisomes are ubiquitous and found across neuronal cell types (Kassmann, 2014), and given the high metabolic demand of not only the photoreceptors, but also the outer and inner plexiform layers (Cringle et al., 2002; Schmidt et al., 2003), the importance of peroxisome function in the retina is likely not limited to a single layer.

Heibler et al. (2014) showed that the peroxisome metabolites, VLCFAs and plasmalogens, were abnormal in PEX1-G844D mouse blood and fibroblasts. We found that in the retina, however, VLCFAs were elevated but plasmalogens were at normal levels (Figure 9D). This suggests that at least at a whole-retina level, the residual function of the PEX1-G844D protein is sufficient for plasmalogen synthesis but cannot maintain VLCFA oxidation. The functional effect of VLCFA accumulation in retina is unknown, but may affect membrane composition (Wangler et al., 2018). It is important to note that there may be localized changes in peroxisome metabolites that cannot be detected at the whole-retina level, as well as disturbances in other peroxisome metabolites that were not measured in this study (such as the methyl branched fatty acids phytanic and pristanic acid).

3.5.3. Clinical implications: The translatability of the Model

Our characterization complements the progression seen in the equivalent human disease, in which patients homozygous for PEX1-G843D exhibit progressive photoreceptor loss, often occurring in the

cone-rich macular region (Majewski et al., 2011; Ventura et al., 2016). Equally, most reported PEX1-G843D patients exhibit retinitis pigmentosa and nyctalopia, suggesting that ZSD features both a cone and rod photoreceptor deterioration (Pakzad-Vaezi and Maberley, 2014; Berendse et al., 2016). Although the mouse model recapitulates cone loss, it does not exhibit a rod photoreceptor loss. However, rod photoreceptor function and structure are severely impaired.

Our in-depth retinal phenotyping in the PEX1-G844D mouse model provides accurate endpoints for preclinical trials. These endpoints include improving or preserving ffERG response, and preventing bipolar cell diminishment. The progressive scotopic ffERG decline suggests a therapeutic window at or before the peak age of 4–6 weeks, during which this decline could be prevented. Although cone cells structure and function are impaired at early age, they remain stable over time, and could also be improved by rescuing peroxisome deficiencies, with functional improvement measured by visual acuity (OKR).

Visual impairment is a major, untreatable handicap for ZSD patients. Small molecule compounds such as the chemical chaperones betaine and arginine, and the flavonoid diosmetin, were shown to improve peroxisome functions in PEX1-G844D patient fibroblast lines (Zhang et al., 2010; Berendse et al., 2013; MacLean et al., 2019), and could be tested *in vivo* using the PEX1-G844D mouse model. It is of note that as the PEX1-G844D protein displays greater stability than its human counterpart (discussed in the above section 3.5.2.), the use of chaperone therapy may not be directly translatable. *In vitro* efficacy assays comparing candidate compounds in mouse and human cells, as well structural comparisons between the mouse and human proteins would provide valuable insights. Finally, the PEX1-G844D retina is an ideal candidate for gene augmentation or gene editing therapy targeted to photoreceptors, which could also be tested for functional efficacy in this model.

Funding

This work was supported by the Canadian Institutes of Health Research to NB [grant numbers 12610 to NB, 34575 to NB and PL, PJT-15629 to J-FB] and the Natural Sciences and Engineering Research Council of Canada to [grant numbers RGPAS 478115-2015/RGPIN2015-06582 to J-FB], and Fonds de Recherche du Québec - Santé [FRQS doctoral training award 32105 to CA].

Declarations of interest

None.

Acknowledgements

We would like to acknowledge Dr. Heidi McBride and Dr. Eric Shoubridge for their helpful discussions of the mitochondrial phenotype in the retinal EM images. We also acknowledge the patients and families affected by ZSD and The Global Foundation for Peroxisomal disorders for inspiring and encouraging us to continue researching these conditions.

Appendix A. Supplementary data

Supplementary data to this article can be found online at https://doi.org/10.1016/j.exer.2019.107713.

References

Argyriou, C., D'Agostino, M.D., Braverman, N., 2016. Peroxisome biogenesis disorders. Transl. Sci. Rare Dis. 1, 111–144.

Barot, M., Gokulgandhi, M.R., Mitra, A.K., 2011. Mitochondrial dysfunction in retinal diseases. Curr. Eye Res. 36, 1069–1077.

Berendse, K., Ebberink, M.S., Ijlst, L., Poll-The, B.T., Wanders, R.J., Waterham, H.R., 2013. Arginine improves peroxisome functioning in cells from patients with a mild peroxisome biogenesis disorder. Orphanet J. Rare Dis. 8, 138.

Berendse, K., Engelen, M., Ferdinandusse, S., Majoie, C.B., Waterham, H.R., Vaz, F.M., Koelman, J.H., Barth, P.G., Wanders, R.J., Poll-The, B.T., 2016. Zellweger spectrum disorders: clinical manifestations in patients surviving into adulthood. J. Inherit. Metab. Dis. 39, 93–106.

Bramall, A.N., Wright, A.F., Jacobson, S.G., McInnes, R.R., 2010. The genomic, biochemical, and cellular responses of the retina in inherited photoreceptor degenerations and prospects for the treatment of these disorders. Annu. Rev. Neurosci. 33, 441–472.

Braverman, N.E., Raymond, G.V., Rizzo, W.B., Moser, A.B., Wilkinson, M.E., Stone, E.M., Steinberg, S.J., Wangler, M.F., Rush, E.T., Hacia, J.G., Bose, M., 2016. Peroxisome biogenesis disorders in the Zellweger spectrum: an overview of current diagnosis, clinical manifestations, and treatment guidelines. Mol. Genet. Metab. 117, 313–321.

Bringmann, A., Iandiev, I., Pannicke, T., Wurm, A., Hollborn, M., Wiedemann, P., Osborne, N.N., Reichenbach, A., 2009. Cellular signaling and factors involved in Müller cell gliosis: neuroprotective and detrimental effects. Prog. Retin. Eye Res. 28, 423–451.

Brown, K.T., 1968. The eclectroretinogram: its components and their origins. Vis. Res. 8, 633–677.

Collins, C.S., Gould, S.J., 1999. Identification of a common PEX1 mutation in Zellweger syndrome. Hum. Mutat. 14, 45–53.

Cringle, S.J., Yu, D.Y., Yu, P.K., Su, E.N., 2002. Intraretinal oxygen consumption in the rat in vivo. Investig. Ophthalmol. Vis. Sci. 43, 1922–1927.

Dick, E., Miller, R.F., 1978. Light-evoked potassium activity in mudpuppy retina: its relationship to the b-wave of the electroretinogram. Brain Res. 154, 388–394.

Dirkx, R., Vanhorebeek, I., Martens, K., Schad, A., Grabenbauer, M., Fahimi, D., Declercq, P., Van Veldhoven, P.P., Baes, M., 2005. Absence of peroxisomes in mouse hepatocytes causes mitochondrial and ER abnormalities. Hepatology 41, 868–878.

Ebberink, M.S., Mooijer, P.A., Gootjes, J., Koster, J., Wanders, R.J., Waterham, H.R., 2011. Genetic classification and mutational spectrum of more than 600 patients with a Zellweger syndrome spectrum disorder. Hum. Mutat. 32, 59–69.

Ebberink, M.S., Csanyi, B., Chong, W.K., Denis, S., Sharp, P., Mooijer, P.A., Dekker, C.J., Spooner, C., Ngu, L.H., De Sousa, C., Wanders, R.J., Fietz, M.J., Clayton, P.T., Waterham, H.R., Ferdinandusse, S., 2010. Identification of an unusual variant peroxisome biogenesis disorder caused by mutations in the PEX16 gene. J. Med. Genet. 47, 608–615.

Falkenberg, K.D., Braverman, N.E., Moser, A.B., Steinberg, S.J., Klouwer, F.C.C., Schlüter, A., Ruiz, M., Pujol, A., Engvall, M., Naess, K., van Spronsen, F., Körver-Keularts, I., Rubio-Gozalbo, M.E., Ferdinandusse, S., Wanders, R.J.A., Waterham, H.R., 2017. Allelic expression imbalance promoting a mutant PEX6 allele causes zellweger spectrum disorder. Am. J. Hum. Genet. 101, 965–976.

Folz, S., Trobe, J., 1991. The peroxisome and the eye. Surv. Ophthalmol. 35, 353–368.

Fransen, M., Lismont, C., Walton, P., 2017. The peroxisome-mitochondria connection: how and why? Int. J. Mol. Sci. 18.

Gärtner, J., Preuss, N., Brosius, U., Biermanns, M., 1999. Mutations in PEX1 in peroxisome biogenesis disorders: G843D and a mild clinical phenotype. J. Inherit. Metab. Dis. 22, 311–313.

Goldfischer, S., Moore, C.L., Johnson, A.B., Spiro, A.J., Valsamis, M.P., Wisniewski, H.K., Ritch, R.H., Norton, W.T., Rapin, I., Gartner, L.M., 1973. Peroxisomal and mitochondrial defects in the cerebro-hepato-renal syndrome. Science 182, 62–64.

Heynen, H., Wachtmeister, L., van Norren, D., 1985. Origin of the oscillatory potentials in the primate retina. Vis. Res. 25, 1365–1373.

Hiebler, S., Masuda, T., Hacia, J.G., Moser, A.B., Faust, P.L., Liu, A., Chowdhury, N., Huang, N., Lauer, A., Bennett, J., Watkins, P.A., Zack, D.J., Braverman, N.E., Raymond, G.V., Steinberg, S.J., 2014. The Pex1-G844D mouse: a model for mild human Zellweger spectrum disorder. Mol. Genet. Metab. 111, 522–532.

Joly, S., Pernet, V., Dorfman, A.L., Chemtob, S., Lachapelle, P., 2006. Light-induced retinopathy: comparing adult and juvenile rats. Investig. Ophthalmol. Vis. Sci. 47, 3202–3212.

Jung, S., Polosa, A., Lachapelle, P., Wintermark, P., 2015. Visual impairments following term neonatal encephalopathy: do retinal impairments also play a role? Investig. Ophthalmol. Vis. Sci. 56, 5182–5193.

Kassmann, C.M., 2014. Myelin peroxisomes - essential organelles for the maintenance of white matter in the nervous system. Biochimie 98, 111–118.

Kiel, J.A., Emmrich, K., Meyer, H.E., Kunau, W.H., 2005. Ubiquitination of the peroxisomal targeting signal type 1 receptor, Pex5p, suggests the presence of a quality control mechanism during peroxisomal matrix protein import. J. Biol. Chem. 280, 1921–1930.

MacLean, G.E., Argyriou, C., Di Pietro, E., Sun, X., Birjandian, S., Saberian, P., Hacia, J.G., Braverman, N.E., 2019 Mar. Zellweger spectrum disorder patient-derived fibroblasts with the PEX1-Gly843Asp allele recover peroxisome functions in response to flavonoids. J. Cell. Biochem. 120 (3), 3243–3258. https://doi.org/10.1002/jcb.27591. Epub 2018 Oct 26.

Majewski, J., Wang, Z., Lopez, I., Al Humaid, S., Ren, H., Racine, J., Bazinet, A., Mitchel, G., Braverman, N., Koenekoop, R.K., 2011. A new ocular phenotype associated with an unexpected but known systemic disorder and mutation: novel use of genomic diagnostics and exome sequencing. J. Med. Genet. 48, 593–596.

Miller, R.F., Dowling, J.E., 1970. Intracellular responses of the Müller (glial) cells of mudpuppy retina: their relation to b-wave of the electroretinogram. J. Neurophysiol. 33, 323–341.

Mohanty, A., McBride, H.M., 2013. Emerging roles of mitochondria in the evolution, biogenesis, and function of peroxisomes. Front. Physiol. 4, 268.

Molotchnikoff, S., Sicard, E., Lachapelle, P., 1987. Modulations of collicular visual responses by acoustic stimuli in rabbits. Neurosci. Res. 4, 385–395.

Neuhaus, C., et al., 2017. Next-generation sequencing reveals the mutational landscape of clinically diagnosed Usher syndrome: copy number variations, phenocopies, a

predominant target for translational read-through, and. Mol Genet Genomic Med 5, 531–552.
Organisciak, D.T., Vaughan, D.K., 2010. Retinal light damage: mechanisms and protection. Prog. Retin. Eye Res. 29, 113–134.
Pakzad-Vaezi, K.L., Maberley, D.A., 2014. Infantile Refsum disease in a young adult: case presentation and brief review. Retin. Cases Brief Rep. 8, 56–59.
Peachey, N.S., Goto, Y., al-Ubaidi, M.R., Naash, M.I., 1993. Properties of the mouse cone-mediated electroretinogram during light adaptation. Neurosci. Lett. 162, 9–11.
Polosa, A., Bessaklia, H., Lachapelle, P., 2017. Light-Induced retinopathy: young age protects more than ocular pigmentation. Curr. Eye Res. 42, 924–935.
Preuss, N., Brosius, U., Biermanns, M., Muntau, A.C., Conzelmann, E., Gartner, J., 2002. PEX1 mutations in complementation group 1 of Zellweger spectrum patients correlate with severity of disease. Pediatr. Res. 51, 706–714.
Prusky, G.T., Alam, N.M., Beekman, S., Douglas, R.M., 2004. Rapid quantification of adult and developing mouse spatial vision using a virtual optomotor system. Investig. Ophthalmol. Vis. Sci. 45, 4611–4616.
Rahim, R.S., Chen, M., Nourse, C.C., Meedeniya, A.C., Crane, D.I., 2016. Mitochondrial changes and oxidative stress in a mouse model of Zellweger syndrome neuropathogenesis. Neuroscience 334, 201–213.
Ratbi, I., Jaouad, I.C., Elorch, H., Al-Sheqaih, N., Elalloussi, M., Lyahyai, J., Berraho, A., Newman, W.G., Sefiani, A., 2016. Severe early onset retinitis pigmentosa in a Moroccan patient with Heimler syndrome due to novel homozygous mutation of PEX1 gene. Eur. J. Med. Genet. 59, 507–511.
Ratbi, I., et al., 2015. Heimler syndrome is caused by hypomorphic mutations in the peroxisome-biogenesis genes PEX1 and PEX6. Am. J. Hum. Genet. 97, 535–545.
Reuber, B.E., Germain-Lee, E., Collins, C.S., Morrell, J.C., Ameritunga, R., Moser, H.W., Valle, D., Gould, S.J., 1997. Mutations in PEX1 are the most common cause of peroxisome biogenesis disorders. Nat. Genet. 17, 445–448.
Salpietro, V., Phadke, R., Saggar, A., Hargreaves, I.P., Yates, R., Fokoloros, C., Mankad, K., Hertecant, J., Ruggieri, M., McCormick, D., Kinali, M., 2015. Zellweger syndrome and secondary mitochondrial myopathy. Eur. J. Pediatr. 174, 557–563.
Schmidt, M., Giessl, A., Laufs, T., Hankeln, T., Wolfrum, U., Burmester, T., 2003. How does the eye breathe? Evidence for neuroglobin-mediated oxygen supply in the mammalian retina. J. Biol. Chem. 278, 1932–1935.
Schwerter, D.P., Grimm, I., Platta, H.W., Erdmann, R., 2017. ATP-driven processes of peroxisomal matrix protein import. Biol. Chem. 398, 607–624.
Slawecki, M.L., Dodt, G., Steinberg, S., Moser, A.B., Moser, H.W., Gould, S.J., 1995. Identification of three distinct peroxisomal protein import defects in patients with peroxisome biogenesis disorders. J. Cell Sci. 108 (Pt 5), 1817–1829.
Smith, C.E., Poulter, J.A., Levin, A.V., Capasso, J.E., Price, S., Ben-Yosef, T., Sharony, R., Newman, W.G., Shore, R.C., Brookes, S.J., Mighell, A.J., Inglehearn, C.F., 2016. Spectrum of PEX1 and PEX6 variants in Heimler syndrome. Eur. J. Hum. Genet. 24, 1565–1571.
Steinberg, S., Chen, L., Wei, L., Moser, A., Moser, H., Cutting, G., Braverman, N., 2004. The PEX Gene Screen: molecular diagnosis of peroxisome biogenesis disorders in the Zellweger syndrome spectrum. Mol. Genet. Metab. 83, 252–263.
Swanson, L.W., 2004. A laboratory guide with printed and electronic templates for data, models and schematic. In: Brain Maps: Structure of the Rat Brain. Elsevier, Amsterdam.
Ventura, M.J., Wheaton, D., Xu, M., Birch, D., Bowne, S.J., Sullivan, L.S., Daiger, S.P., Whitney, A.E., Jones, R.O., Moser, A.B., Chen, R., Wangler, M.F., 2016. Diagnosis of a mild peroxisomal phenotype with next-generation sequencing. Mol Genet Metab Rep 9, 75–78.
Walter, C., Gootjes, J., Mooijer, P.A., Portsteffen, H., Klein, C., Waterham, H.R., Barth, P.G., Epplen, J.T., Kunau, W.H., Wanders, R.J., Dodt, G., 2001. Disorders of peroxisome biogenesis due to mutations in PEX1: phenotypes and PEX1 protein levels. Am. J. Hum. Genet. 69, 35–48.
Wanders, R.J., Waterham, H.R., 2006. Biochemistry of mammalian peroxisomes revisited. Annu. Rev. Biochem. 75, 295–332.
Wangler, M.F., Hubert, L., Donti, T.R., Ventura, M.J., Miller, M.J., Braverman, N., Gawron, K., Bose, M., Moser, A.B., Jones, R.O., Rizzo, W.B., Sutton, V.R., Sun, Q., Kennedy, A.D., Elsea, S.H., 2018. A metabolomic map of Zellweger spectrum disorders reveals novel disease biomarkers. Genet. Med. 20, 1274–1283.
Zaki, M.S., Heller, R., Thoenes, M., Nürnberg, G., Stern-Schneider, G., Nürnberg, P., Karnati, S., Swan, D., Fateen, E., Nagel-Wolfrum, K., Mostafa, M.I., Thiele, H., Wolfrum, U., Baumgart-Vogt, E., Bolz, H.J., 2016. PEX6 is expressed in photoreceptor cilia and mutated in deafblindness with enamel dysplasia and microcephaly. Hum. Mutat. 37, 170–174.
Zhang, R., Chen, L., Jiralerspong, S., Snowden, A., Steinberg, S., Braverman, N., 2010. Recovery of PEX1-Gly843Asp peroxisome dysfunction by small-molecule compounds. Proc. Natl. Acad. Sci. U. S. A. 107, 5569–5574.